

Flight Test Bed for Visual Tracking of Small UAVs

Lili Ma, Vahram Stepanyan, Chengyu Cao, Imraan Faruque,
Craig Woolsey and Naira Hovakimyan

Dept. of Aerospace and Ocean Engineering, Virginia Tech, Blacksburg, VA 24061, USA.

This paper describes the development of an unmanned aerial vehicle (UAV) system, which will be used to demonstrate multiple-vehicle flight control algorithms. Planned demonstrations include vehicle coordination experiments involving autonomous air, ground, and marine vehicles. More immediately, a system of two UAVs will be used to demonstrate adaptive visual tracking algorithms. To speed development time, critical hardware such as the aircraft autopilots and self-stabilizing gimballed camera system are purchased commercially. These systems are being installed in a commonly available hobby industry airframe. This paper describes component selection and high-level integration and results from early flight tests. The paper also describes the vision-based target tracking algorithm to be demonstrated using this system.

I. Introduction

MILITARY and civilian applications of unmanned air vehicles (UAVs) have dramatically increased in recent years. Within the spectrum of existing UAVs, small, low-cost vehicles are finding use in a number of niche applications. Small UAVs are especially appealing for use in research projects focused on autonomous vehicle coordination because they are inexpensive to build and repair. Moreover, there are highly capable, commercially available autopilots which can transform an ordinary radio control (R/C) aircraft into a sophisticated flight control system test bed. Experimental systems play a crucial role in validating newly developed control algorithms. This paper describes a UAV system developed by the Virginia Center for Autonomous Systems (VaCAS) at Virginia Tech. While the system was developed with a view toward flexibility, anticipating a wide range of possible applications, an immediate objective is to implement the vision-based target tracking guidance algorithms described in Refs. 1–4. We note that these algorithms couple estimation and control to achieve the control objective. Separately, an alternative control algorithm is developed at VaCAS that assumes a custom-built gimbal for the camera, the open-loop control of which enables decoupling of estimation from feedback control 5.

Development of the VaCAS UAV system was guided, in part, by similar UAV systems developed at the Naval Postgraduate School (NPS) and Brigham Young University (BYU). The rapid flight test prototyping system developed by NPS, as documented in Refs. 6, 7, has served as the primary model for the VaCAS UAV system. The NPS system includes: 1) a commercial off-the-shelf (COTS) autopilot system, the Piccolo autopilot from Cloud Cap Technology 8, 2) a ground control system for UAV guidance and navigation, 3) an on-board camera with a custom pan-tilt unit driven from the ground station, and 4) a COTS image processing software package, called PerceptiVU 9, running on a separate ground computer. Video from the onboard camera is transmitted to the ground using a 2.4 GHz wireless data link. A 900 MHz telemetry link operates between the autopilot and the ground control station. Development of serial communication interfaces is documented in Ref. 10. More details about the system setup can be found in Refs. 6, 7.

The UAV test bed developed at the MAGICC Lab at BYU is quite similar to the NPS system. The BYU system was also developed with a view toward cooperative control experiments involving multiple vehicles 11, 12. The setup includes components similar to the four described above for the NPS system, although MAGICC Lab researchers developed most of these components in-house. Developing custom hardware and software gives researchers more freedom to develop and implement control algorithms and, in some cases, may lead to new commercial products. On the other hand, it takes considerable time and breadth of expertise. In developing a UAV system for VaCAS, the research objectives and project time-line imposed a trade-off between system flexibility and rapid development. Ultimately, it was decided that the VaCAS

system should include a COTS autopilot system and gimballed camera system. Image processing software is being developed in-house.

The paper is organized as follows. In Section II, we describe the system hardware and software and include data from preliminary test flights. Section III formulates a specific vision-based UAV tracking problem; the control algorithm is presented in Section IV. Simulation results are described in Section V. We give concluding remarks and describe plans for continuing work in Section VI.

II. Test Bed

Vision-based air-to-air tracking experiments are scheduled for fall 2006. At time of writing, all major components of the UAV test bed have been selected and most of these components have been purchased and integrated. This section describes the ongoing development effort, starting with an overview of the system architecture and followed by a more detailed discussion of each key component.

II.A. Overview of the System Architecture

Observing a trade-off between ease of development and system flexibility, we have chosen to purchase COTS hardware, including the airframe, autopilot system, and gimballed vision system. The architecture will be similar to the NPS setup described in Refs. 6,7, but possibly with a single ground station performing both UAV guidance and navigation tasks and image processing functions. The architecture is shown in Figure 1. A modified R/C scale fix-wing aircraft houses an autopilot and a gimballed camera as its primary payloads. Video from the onboard camera is transmitted to the ground station for processing via a 2.4 GHz wireless link. Images are processed on the ground station, generating essential information about the target, such as its centroid and estimated dimensions. This information is passed to the the guidance and navigation module, which then calculates the desired aircraft trajectory. The appropriate guidance commands are passed to the UAV through a ground-based telemetry and control system purchased with the autopilot. The servo-actuated gimbal for the video camera is automatically adjusted from the ground based on locally computed information about the relative motion of the target with respect to the follower. The gimbal is controlled through a separate communication channel which is independent of the autopilot system. For safety, the autopilot system allows a human supervisor to intervene and take manual control of the vehicle.

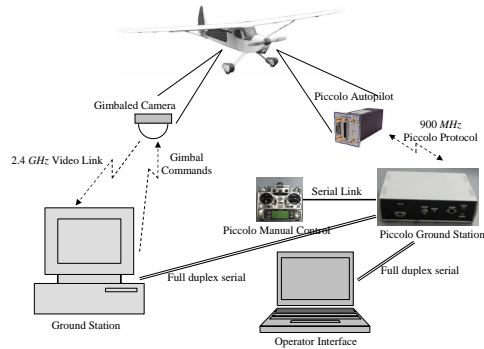


Figure 1. Flight test setup.

If early field tests indicate that the image processing algorithms are too computationally expensive to be implemented along with the control algorithm in a single computer, the configuration shown in Figure 1 can be easily modified to include a separate ground-based image-processing computer. Outputs from the image processing module can be provided to the control module through direct ethernet or serial link.

II.B. Airframe and Propulsion

The aerial vehicle is built around a commercial R/C airframe known as the Sig Rascal 110. This is a high-wing, box-fuselage aircraft with a wing span of 110 inches. The airframe is pictured in Figure 2. This airframe was selected for several reasons, but chiefly for its size and payload capability. The Rascal 110 is one of the largest R/C airplanes available. With the standard R/C configuration weight of approximately

13 to 14 pounds (depending on the amount of fuel remaining in the tank), the aircraft has a wing loading of only 19 to 22 oz/ft², which is reflected by its relatively slow flight. Because it is so large, the dynamic modes are significantly slower than those of a smaller UAV, a fact which is advantageous for control algorithms that require extensive processing.



Figure 2. Sig Rascal 110 base airframe.

Model airplanes and many small UAVs are normally powered by a mixture of methanol (70 ~ 90% by volume), nitromethane (2 ~ 15% by volume), and castor oil (18 ~ 23% by volume). These engines are known as “glow engines” because a glow plug is used to ignite the mixture. The fuel consumption is relatively high, however. For this airframe and payload, the aircraft would be required to carry significant fuel reserves or would be constrained to short flight durations. To circumvent this problem for aircraft of this size, many R/C pilots use small gasoline “chainsaw-type” engines. These engines have a longer runtime, but are slightly heavier and use a spark plug-based ignition system that can create radio interference.

A less common propulsion method involves using diesel fuel. Although two-stroke diesel engines can be messy, they boast a high torque output and no spark or glow plugs. One may typically use an engine with 2/3 the displacement of a comparable glow or gasoline engine, significantly reducing weight. The UAVs in the test bed described here use an OS MAX engine with a 1.08 in³ displacement. The engine is actually a glow engine which has been converted to use diesel fuel by swapping the standard head for one manufactured by Davis Diesel Development ¹³. The converted engine generates ample power with a significantly reduced propulsion system weight. An additional advantage is that diesel engines are less sensitive to back pressure, which allows the exhaust to be ducted through the interior of the airplane and vented out the tail. Since two-stroke engines (whether, glow, gasoline, or diesel) normally vent a significant amount of oil through their exhaust, there is a tremendous advantage to locating the engine exhaust downstream of sensors and actuators, particularly a gimballed video system.

II.C. Avionics

Cloud Cap Technology’s Piccolo Plus avionics suite was selected as the onboard autopilot. The system comprises a vehicle-mounted computer and sensor suite and a ground station which provides GPS position correction and a user interface. The on-board unit is highly integrated, combining three angular rate gyros, three accelerometers, a GPS unit, pitot/static air pressure sensors, a 40 MHz PowerPC processor, and a UHF data modem in a ruggedized enclosure. The manufacturer also makes its autopilot source code available for purchase, allowing a user to load a newly developed controller in place of the factory-supplied controller.

At the time of writing, the avionics package has been integrated into the airframe and motion data have been collected for several manual and autonomous flights in order to verify the sensing system’s accuracy. Figure 3 shows plots of data logs, including 3-D position, from GPS, pressure and GPS altitude, airspeed and acceleration. The simple test flight included a takeoff, downwind leg, and landing. Significant events (such as take-off and landing) are obvious from the data. The data in Figure 3 (a) were taken from the onboard GPS receiver. Latitude/longitude data were converted to a local right-handed (East-North-up) coordinate frame with distances measured in feet from the starting location. In Figure 3 (b), two altitude plots are shown; one is based on static pressure, relative to the standard atmosphere, while the other is GPS-measured altitude. The plot illustrates the inherent noise in GPS altitude measurements, but the trends show reasonable agreement. Altitude measurements are Kalman filtered with a much higher degree of confidence in barometric altitude (i.e., low noise covariance) as compared with GPS. The coarse GPS altitude readings are therefore not a significant performance handicap. Having demonstrated the sensing system’s accuracy, a careful, well-planned procedure is now being followed to transition the UAV to autonomous flight.

Earlier it was mentioned that this aircraft flies slowly in comparison to smaller, more common R/C aircraft. The airspeed plot in Figure 3 (c) shows an average airspeed of approximately 9 m/s (roughly 20 mph). Figure 3 (d) shows the recorded accelerometer data, expressed in traditional body-fixed stability axes.

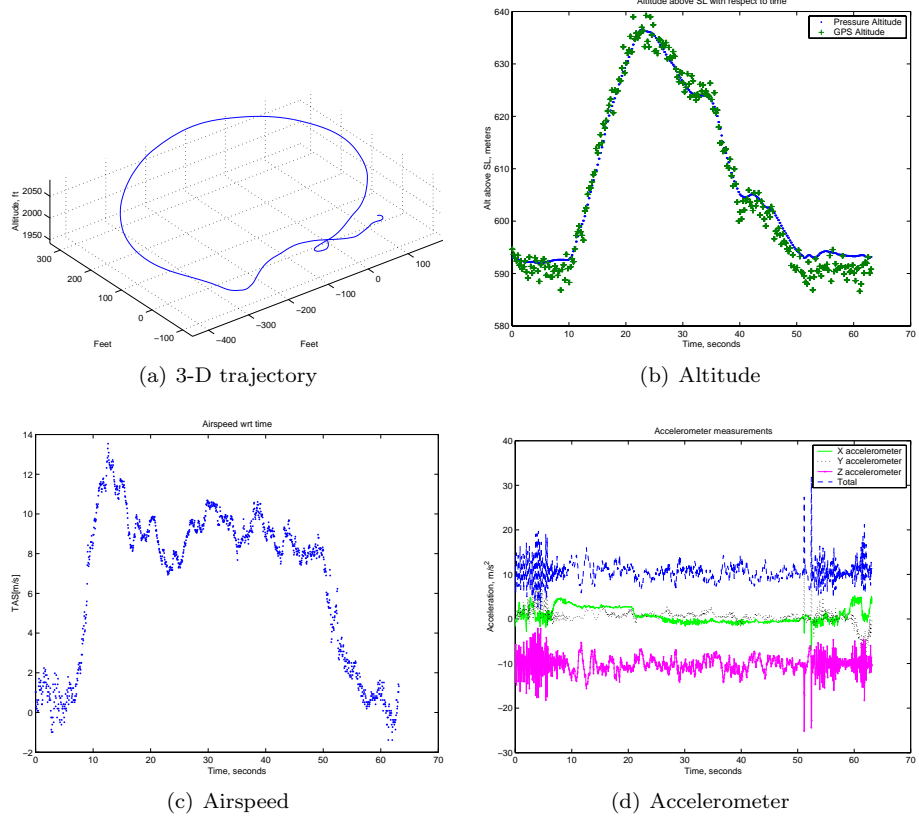


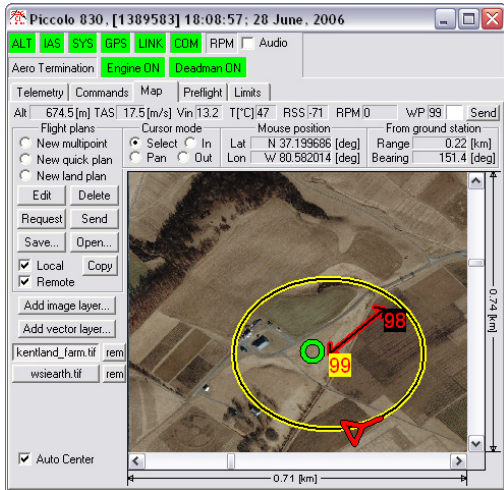
Figure 3. Data logs for an example flight.

These flight data were collected before all of the sensors were zeroed; a steady state bias was removed during post-processing for the data shown in Figure 3 (c).

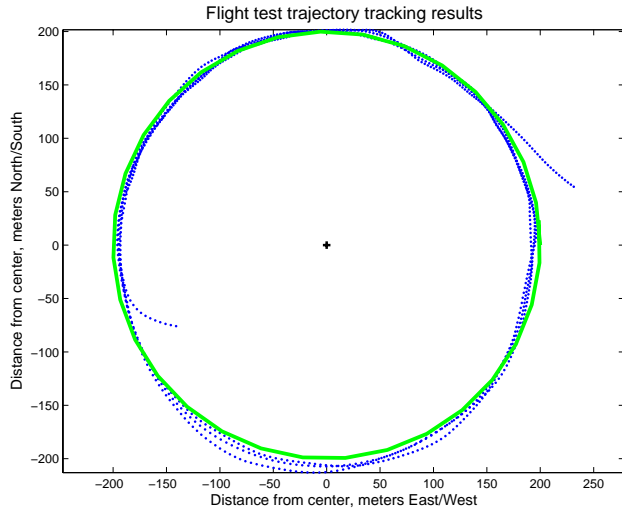
Multiple autonomous flights have also been achieved on a day-to-day basis, where the given flight plans have included circles, rectangles, and user-specified way points. Figure 4 (a) shows a screen shot of the Piccolo operator interface during one example autonomous flight when the aircraft follows a circle, where the small green circle indicates the location of the ground station, the number “99” indicates the center of the circle, and the vector from “99” to “98” shows the radius of the circle. The desired trajectory is shown via the yellow circle. The red arrow indicates the position of the aircraft at the time of the screen shot. Figure 4 (b) shows the desired and actual trajectories with the desired trajectory plotted in green and the actual plotted in blue.

II.D. Onboard Vision System

To save time and effort in developing the test bed, we have focused on purchasing COTS gimbal products. The search for small, light-weight, automatically stabilized gimbal systems led to three viable options: the Controp D-STAMP¹⁴, the Tenix¹⁵, and the Cloud Cap Technology TASE gimbal systems¹⁶. After comparing features and cost, it was determined that the Cloud Cap system best suits the needs of this project. The device is expected to become commercially available in late summer 2006. The Cloud Cap TASE gimbal is designed to have an overall package size of $5 \times 4 \times 7$ inches. It weighs less than 1Kg and has 360° continuous azimuth and 23° -up and 203° -down tilt. The gimbal will be controlled through a stand-alone serial communication link (using wireless modems), which is independent of the Piccolo autopilot link used for motion data telemetry and for guidance and navigation. At the same time, to progress in our project, several Black Widow AV 600mw Brown Bag Kits¹⁷ have been purchased, and one has been installed/fixed on the aircraft for computer vision algorithm development.



(a) Piccolo Operator Interface



(b) Desired and Actual Trajectories

Figure 4. Desired and actual trajectories for an example autonomous flight when the aircraft follows a circle.

II.E. Ground Station

Intensive image processing and control computation tasks will be performed on the ground station. Inputs to the ground station shall include the wirelessly transmitted video imagery from the onboard camera and the aircraft motion data, (including the gimbal attitude). The ground station generates the guidance commands for the aircraft and sends them to the onboard Piccolo autopilot through the Piccolo ground station. The Piccolo communication SDK will be used for this purpose. The gimbal will be controlled through another independent wireless serial communication link. Right now, the image processing and communications to the Piccolo ground station are implemented in C/C++ on the Windows operating system.

III. Tracking Problem with Fixed Camera

In this section, a target tracking problem using visual information from a single camera fixed on the UAV, called the follower, is formulated. Without loss of generality we assume that the optical axis of the camera is aligned with the follower's longitudinal x_B -axis of the body frame $F_B = \{x_B, y_B, z_B\}$, and the optical center of it is fixed at the center of gravity of the follower. Otherwise, the coordinates of the optical center and the direction of the optical axis could be taken into account in the equations of relative motion presented. Then the body frame can be chosen coincident with the camera frame; see Figure 5 (a). It is assumed that the image processing algorithm associated with the camera provides three measurements in real time. These are the pixel coordinates of the image centroid (y_I, z_I) in the image plane I and the image length b_I in pixels; see Figure 5 (b). Assuming that the camera focal length l is known, the bearing angle λ , and the elevation angle ϑ can be expressed via the measurements through the geometric relationships

$$\tan \lambda = \frac{y_I}{l}, \quad \tan \vartheta = \frac{z_I}{\sqrt{l^2 + y_I^2}}. \quad (1)$$

In a kinematic setting the equation of motion for the flying target is given by:

$$\dot{\mathbf{R}}_T^E(t) = \mathbf{V}_T^E(t), \quad \mathbf{R}_T^E(0) = \mathbf{R}_{T_0}^E, \quad (2)$$

where $\mathbf{R}_T^E(t) = [x_T^E(t) \ y_T^E(t) \ z_T^E(t)]^\top$ and $\mathbf{V}_T^E(t) = [V_{T_x}^E(t) \ V_{T_y}^E(t) \ V_{T_z}^E(t)]^\top$ are respectively the position and velocity vectors of the target's center of gravity in some inertial frame $F_E = \{x_E, y_E, z_E\}$. The follower is described by the equation

$$\dot{\mathbf{R}}_F^E(t) = \mathbf{V}_F^E(t), \quad \mathbf{R}_F^E(0) = \mathbf{R}_{F_0}^E, \quad (3)$$

where $\mathbf{R}_F^E(t) = [x_F^E(t) \ y_F^E(t) \ z_F^E(t)]^\top$ and $\mathbf{V}_F^E(t) = [V_{F_x}^E(t) \ V_{F_y}^E(t) \ V_{F_z}^E(t)]^\top$ are respectively the follower's position and velocity vectors in the same inertial frame F_E .

We assume that the follower can measure its own states in addition to the visual measurements, but does not have any knowledge about the target's size or state, other than the camera image. The target's relative position with respect to the follower is given by the inertial vector

$$\mathbf{R}^E = \mathbf{R}_T^E - \mathbf{R}_F^E, \quad (4)$$

and the relative motion is:

$$\dot{\mathbf{R}}^E(t) = \mathbf{V}_T^E(t) - \mathbf{V}_F^E(t), \quad \mathbf{R}^E(0) = \mathbf{R}_0, \quad (5)$$

where the initial condition is given by $\mathbf{R}_0^E = \mathbf{R}_{T_0}^E - \mathbf{R}_{F_0}^E$. The objective is to find a guidance law $\mathbf{V}_F^E(t)$ for the follower in order to maintain a pre-specified relative position described by $R_c(t)$, $\lambda_c(t)$, $\vartheta_c(t)$ given in the body frame F_B . This is a challenging control problem, since the relative range $R(t) = \|\mathbf{R}^E(t)\|$ is not measured directly. It is related to the image plane measurements $(y_I(t), z_I(t), b_I)$ via the equation

$$R = \frac{b}{b_I} \sqrt{l^2 + y_I^2 + z_I^2} \triangleq ba_I. \quad (6)$$

Here $b > 0$ is the size of the target that is assumed to be constant but otherwise unknown to the follower.

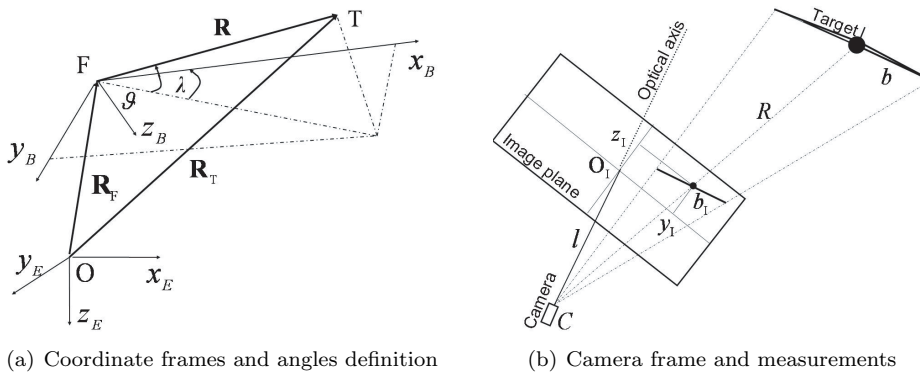


Figure 5. Coordinate illustrations.

It is worth noting that the dynamic equation (5) is written in the inertial frame F_E , the reference commands $R_c(t)$, $\lambda_c(t)$, $\vartheta_c(t)$ are given in the body frame F_B and the visual measurements are taken in the image plane. To unify all the quantities of interest we introduce the scaled relative position vector $\mathbf{r}^E(t) = \frac{\mathbf{R}^E(t)}{b}$, the dynamics of which are written as

$$\dot{\mathbf{r}}^E(t) = \frac{1}{b} [\mathbf{V}_T^E(t) - \mathbf{V}_F^E(t)], \quad \mathbf{r}^E(0) = \mathbf{r}_0^E, \quad (7)$$

where $\mathbf{r}_0^E = \frac{\mathbf{R}_0^E}{b}$. Using the coordinate transformation matrix $L_{F_B/E}$ from the inertial frame F_E to the body frame F_B , we can write $\mathbf{r}^E = L_{B/E}^\top \mathbf{r}^B$, where components of \mathbf{r}^B are related to the visual measurements via the following algebraic expressions:

$$\begin{aligned} r_x^B &= a_I \cos \vartheta \cos \lambda, \\ r_y^B &= a_I \cos \vartheta \sin \lambda, \\ r_z^B &= -a_I \sin \vartheta. \end{aligned} \quad (8)$$

Hence the vector \mathbf{r}^E is available for feedback. Similarly, the reference commands $R_c(t)$, $\lambda_c(t)$, $\vartheta_c(t)$ can be translated to the inertial frame as

$$\begin{bmatrix} r_{xc}^E(t) \\ r_{yc}^E(t) \\ r_{zc}^E(t) \end{bmatrix} = \frac{R_c(t)}{b(t)} L_{B/E}^\top \begin{bmatrix} \cos \vartheta_c(t) \cos \lambda_c(t) \\ \cos \vartheta_c(t) \sin \lambda_c(t) \\ -\sin \vartheta_c(t) \end{bmatrix}, \quad (9)$$

Here we notice that for the given bounded commands $R_c(t)$, $\lambda_c(t)$ and $\vartheta_c(t)$ the reference vector $\xi_c = [r_{xc}^E(t) \ r_{yc}^E(t) \ r_{zc}^E(t)]^\top$ is bounded.

The problem is reduced to designing a guidance command $\mathbf{u}(t) = \mathbf{V}_F^E(t)$ for the follower, using the available signal $\xi(t) = \mathbf{r}^E(t)$, such that the trajectories of the system

$$\dot{\xi}(t) = \frac{1}{b}[-\mathbf{u}(t) + \mathbf{V}_T^E(t)], \quad (10)$$

asymptotically track the bounded reference command ξ_c , regardless of the realization of the target's motion. Thus we have a simultaneous tracking and disturbance rejection problem for a multi-input multi-output linear system (10), with positive but unknown high frequency gain in each control channel, that has to be solved for a reference signal $\xi_c(t)$ that depends on the unknown parameter b via the expressions in equation (9).

IV. Guidance Law

The problem formulated above has been solved in Ref. 4 when the target's velocity is subject to the following assumption.

Assumption 1 Assume that the target's inertial velocity $\mathbf{V}_T^E(t)$ is a bounded function of time and has bounded time derivative, i.e. $\mathbf{V}_T^E(t), \dot{\mathbf{V}}_T^E(t) \in \mathcal{L}_\infty$. Further, assume that any maneuver made by the target is such that the velocity returns to some constant value in finite time or asymptotically in infinite time with a rate sufficient for the integral of the magnitude of velocity change to be finite, that is $\mathbf{V}_T^E(t) = \mathbf{V}_s + \Delta\mathbf{V}_T(t)$, where \mathbf{V}_s is a constant and $\Delta\mathbf{V}_T(t) \in \mathcal{L}_2$.

Since b is a constant, this assumption can be formulated for the function $\mathbf{d}(t) = \frac{1}{b(t)}\mathbf{V}_T^E(t)$ as follows:

$$\mathbf{d}(t) = \mathbf{d}_s + \boldsymbol{\delta}(t), \quad (11)$$

where $\mathbf{d}_s \in \mathbb{R}^3$ is an unknown but otherwise constant vector, and $\boldsymbol{\delta}(t) \in \mathcal{L}_2$ is an unknown time-varying term. Applying the corollary of Barbalat's lemma from Ref. 18 (p.19), we conclude that

$$\boldsymbol{\delta}(t) \rightarrow 0, \quad t \rightarrow \infty. \quad (12)$$

It is interesting to notice that obstacle avoidance maneuvers by the target verify this assumption, provided that after the maneuvers the target velocity returns to a constant in finite time or asymptotically in infinite time subject to \mathcal{L}_2 constraint. The guidance law derived in Ref. 4 is given by the equation

$$\begin{aligned} \mathbf{u}(t) &= \hat{b}(t)\mathbf{g}(t) \\ \mathbf{g}(t) &= k\mathbf{e}(t) + \hat{\mathbf{d}}(t) - \dot{\hat{\xi}}_c(t) \\ \dot{\hat{b}}(t) &= \sigma \text{Proj}(\hat{b}(t), \mathbf{e}^\top(t)\mathbf{g}(t)), \quad \hat{b}(t_0) = \hat{b}_0 > 0 \\ \dot{\hat{\mathbf{d}}}(t) &= G\text{Proj}(\hat{\mathbf{d}}(t), \mathbf{e}(t)), \quad \hat{\mathbf{d}}(t_0) = \hat{\mathbf{d}}_0, \end{aligned} \quad (13)$$

where $\mathbf{e}(t) = \xi(t) - \xi_c(t) \in \mathbb{R}^3$ is the tracking error, $\hat{b}(t) \in \mathbb{R}$ and $\hat{\mathbf{d}}(t) \in \mathbb{R}^3$ are the estimates of the unknown parameter b and the nominal disturbance \mathbf{d} respectively, $k > 1/4$, $\sigma > 0$ are constants (adaptation gain), G is a positive definite matrix (adaptation gain), and $\text{Proj}(\cdot, \cdot)$ is the Projection operator¹⁹, that guarantees known conservative bounds $0 < b_{\min} \leq \hat{b}(t) \leq b_{\max}$, and $\|\hat{\mathbf{d}}(t)\| \leq d^*$. In equation (13), $\hat{\xi}_c$ is the estimated reference command given by

$$\hat{\xi}_c = \begin{bmatrix} \hat{\xi}_{cx}(t) \\ \hat{\xi}_{cy}(t) \\ \hat{\xi}_{cz}(t) \end{bmatrix} = \frac{R_c(t)}{\hat{b}(t)} \begin{bmatrix} \cos(\vartheta_c(t)) \cos(\lambda_c(t)) \\ \cos(\vartheta_c(t)) \sin(\lambda_c(t)) \\ -\sin(\vartheta_c(t)) \end{bmatrix}. \quad (14)$$

The guidance law $\mathbf{u}(t)$ in equation (13) guarantees asymptotic tracking of the reference trajectory $\hat{\xi}_c(t)$. It has been shown that in the case of formation flight with constant commands R_c , λ_c , ϑ_c the true reference command $\xi_c(t)$ is guaranteed to be tracked asymptotically in the presence of the excitation signal that is added to relative range command R_c , when also the parameter estimates converge to the true values.

The amplitude of the excitation signal can be controlled according to the intelligent excitation technique introduced in Ref. 1. It is done by choosing the amplitude dependent upon tracking error. Below in simulations we incorporate this technique to ensure parameter convergence.

In the case of target interception, parameter convergence is not required since the reference command is $\hat{\xi}_c(t) = \xi_c(t) = 0$. Therefore, the guidance law $\mathbf{u}(t)$ in equation (13) always guarantees target interception.

V. Simulation

In simulations, the tracking error is formed by using a_I and angles λ, ϑ that relate to the measurements ($y_I(t), z_I(t), b_I(t)$) via the equations (1) and (6). The reference command is formulated according to equation (14), where the signal $\hat{b}(t)$ is generated according to the adaptive law in equation (13) with the initial estimation of $\hat{b}(0) = 1.5\text{ft}$. The excitation signal is introduced following Ref. 1 with the following amplitude:

$$a(t) = \begin{cases} k_1, & t \in [0, T) \\ \min\{k_2 \int_{t-T}^t e^\top(\tau) e(\tau) d\tau, k_1 - k_3\} + k_3, & t \geq T, \end{cases}$$

where $e(t)$ is the tracking error, $T = \frac{2\pi}{\omega}$ is the period of the excitation signal $a(t) \sin(\omega t)$, $k_i > 0$, $i = 1, 2, 3$ are design constants set to $T = 3\text{sec}$, $k_1 = 0.4$, $k_2 = 500$, $k_3 = 0.0002$. In the simulation scenario a target of length $b = 3\text{ft}$ starts moving with the constant velocity $V_{Tx} = 30\text{ft/sec}$, $V_{Ty} = V_{Tz} = 0$ and follows the velocity profile displayed in Figure 7 (b) (the analytic expressions are not presented). The target's velocity can be represented as $\mathbf{V}_T(t) = b(\mathbf{d} + \tilde{\mathbf{d}}(t))$, where $\mathbf{d} = [10 \ 0 \ 0]^\top \text{ft/sec}$ is a constant term and $\tilde{\mathbf{d}}(t)$ is a time-varying term that captures all the maneuvers and the asymptotically decaying perturbations and satisfies the inequalities $\|\tilde{\mathbf{d}}(t)\|_\infty \leq 40$, $\|\dot{\tilde{\mathbf{d}}}(t)\|_\infty \leq 7.5\pi$ and $\tilde{\mathbf{d}}(t) \in \mathcal{L}_2$. We recall that $\dot{\tilde{\mathbf{d}}}(t)$ represents the target acceleration, and, hence, during the maneuvers it is bounded. The follower is commanded to maintain a relative range of $R_c = 15\text{ft}$, bearing angle of $\lambda_c = 15^\circ$ and relative elevation of $\vartheta_c = 0^\circ$. Initial conditions are chosen to be $x_{B_0} = 36\text{ft}$, $y_{B_0} = 21\text{ft}$, $z_{B_0} = -15\text{ft}$. The guidance law is implemented according to equation (13) with $k = 3.5$. Simulation results are shown in Figures 6, 7, and 8. Figure 6 shows the system output convergence, where (b) is the zoomed version of the tracking performance over a time period when excitation is active. The parameter convergence is shown in Figure 7 (a). Figure 7 (b) shows that the guidance law is able to capture the target's velocity profile with a certain lag, which disappears when the target returns to the nominal velocity. The large fluctuations in the estimation of \mathbf{d}_0 are due to the presence of target acceleration during the maneuvers. We note that the magnitude of the velocity varies in $[-40 \ 40]\text{ft/sec}$. The target's size estimation gradually converges to the true value. The range discrepancy is visible only during the target's maneuvers and vanishes as the target returns to its nominal motion. The bearing angle has big fluctuations due to the target's turning maneuvers, which are assumed to stay in the field of view of the aerial vehicle during the entire task. Figure 8 demonstrates the amplitude of intelligent excitation. As it can be seen from the figure, excitation is activated only during the target maneuvers and vanishes as the target returns to its nominal motion.

VI. Concluding Remarks

An automated vision-based target tracking system is introduced. The flight test bed is still being developed; data from preliminary flight tests are included here. This flexible UAV system test bed will provide the ability to implement and test a variety of UAV flight control tasks, including multiple-vehicle coordination experiments and vision-based flight control. Experiments involving autonomous visual tracking of manually piloted UAV are ongoing. The vision-based target tracking algorithm that will be implemented was first presented in an earlier paper, but is revisited here, along with new simulation results illustrating its viability. Of course, the algorithm can not be directly implemented as presented because the camera is assumed to be fixed with respect to the airframe. Ongoing efforts include the adaptation of the visual tracking algorithm presented here to a camera which is mounted on a servo-actuated 2-axis gimbal.

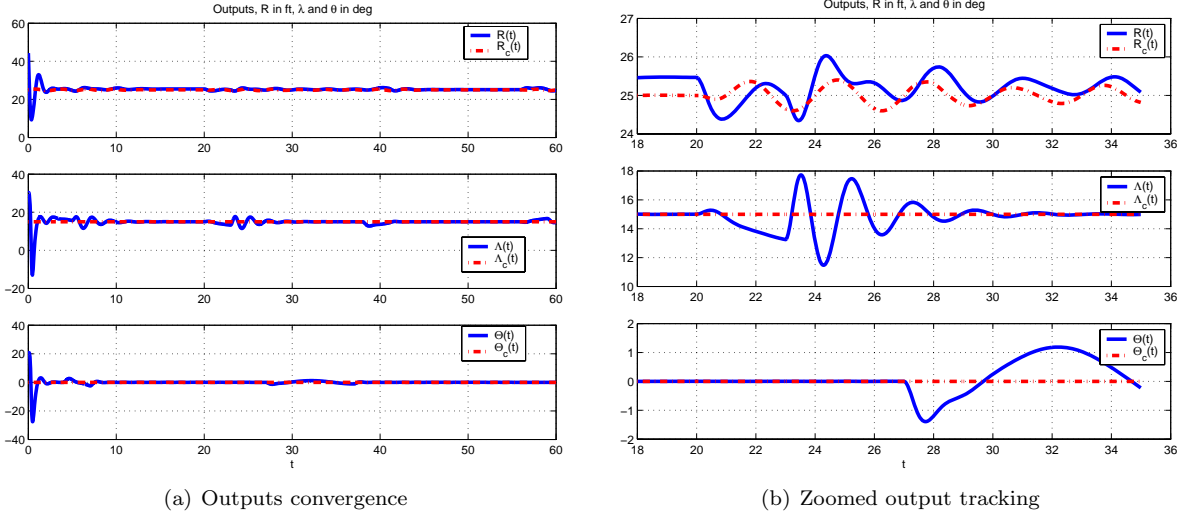


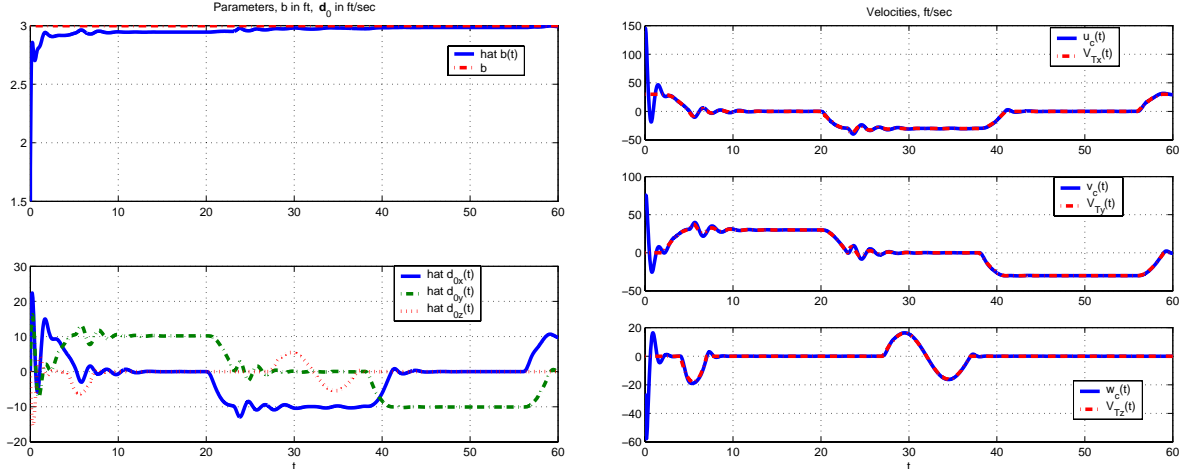
Figure 6. System output convergence.

Acknowledgments

The authors gratefully acknowledge the advice and guidance of V. Dobrokhodov of NPS. This work was sponsored in part by ONR Grant #N00014-05-1-0828 and AFOSR MURI subcontract F49620-03-1-0401.

References

- ¹Cao, C. and Hovakimyan, N., "Vision-Based Aerial Tracking Using Intelligent Excitation," *American Control Conference*, Portland, OR, USA, June 8-10 2005, pp. 5091–5096.
- ²Cao, C. and Hovakimyan, N., "Vision-Based Aerial Tracking using Intelligent Excitation," *Submitted to Automatica*, 2005.
- ³Stepanyan, V. and Hovakimyan, N., "A Guidance Law for Visual Tracking of a Maneuvering Target," *American Control Conference*, Minneapolis, Minnesota, June 14-16 2006, pp. 2850–2855.
- ⁴Stepanyan, V. and Hovakimyan, N., "Adaptive Disturbance Rejection Guidance Law for Visual Tracking of a Maneuvering Target," *AIAA Guidance, Navigation, and Control Conference and Exhibit*, San Francisco, CA, Aug. 15-18 2005.
- ⁵Cao, C., Hovakimyan, N., and Evers, J., "Active Control of Visual Sensor for Aerial Tracking," *AIAA Guidance, Navigation, and Control Conference and Exhibit*, Keystone, Colorado, USA, Aug. 21-24 2006.
- ⁶Wang, I. H., Dobrokhodov, V. N., Kaminer, I. I., and Jones, K. D., "On Vision-Based Target Tracking and Range Estimation for Small UAVs," *AIAA Guidance, Navigation, and Control Conference and Exhibit*, San Francisco, CA, Aug. 15-18 2005.
- ⁷Kaminer, I. I., Yakimenko, O. A., Dobrokhodov, V. N., and Jones, K. D., "Rapid Flight Test Prototyping System and the Fleet of UAV's and MAVs at the Naval Postgraduate School," *AIAA 3rd "Unmanned Unlimited" Technical Conference, Workshop and Exhibit*, Chicago, Illinois, Sep. 20-23 2004.
- ⁸"Cloud Cap Piccolo," <http://www.cloudcaptech.com/piccolo.htm>.
- ⁹"PerceptiVU," <http://www.perceptivu.com/>.
- ¹⁰Dobrokhodov, V. and Lizarrage, M., "Developing Serial Communication Interfaces for Rapid Prototyping of Navigation and Control Tasks," *AIAA Modeling and Simulation Technologies Conference and Exhibit*, San Francisco, CA, Aug. 15-18 2005.
- ¹¹Quigley, M., Goodrich, M. A., Griffiths, S., Eldredge, A., and Beard, R. W., "Target Acquisition, Localization, and Surveillance using a Fixed-Wing Mini-UAV and Gimbaled Camera," *IEEE International Conference on Robotics and Automation*, Barcelona, Spain, April 18-22 2005.
- ¹²McLain, T. and Beard, R., "Unmanned Air Vehicle Testbed for Cooperative Control Experiments," *American Control Conference*, Boston, MA, June 30-July 2 2004, pp. 5327–5331.
- ¹³"Davis Diesel Development," <http://davisdieseldevelopment.com/>.
- ¹⁴"Controp D-STAMP," <http://www.controp.com/PRODUCTS/SPSproducts/Products-SPS-d-stamp.asp>.
- ¹⁵"Tenix," <http://www.tenix.com/PDFLibrary/274.pdf>.
- ¹⁶"Cloud Cap Gimbal," <http://www.cloudcaptech.com/gimbal.htm>.
- ¹⁷"Black Widow AV," <http://www.blackwidowav.com/brownbagkits.html>.
- ¹⁸Sastry, S. and Bodson, M., *Adaptive Control: Stability, Convergence, and Robustness*, Prentice-Hall, 1989.



(a) Parameters convergence

(b) The follower's velocity vs the target's velocity

Figure 7. Parameters convergence and tracking velocities.

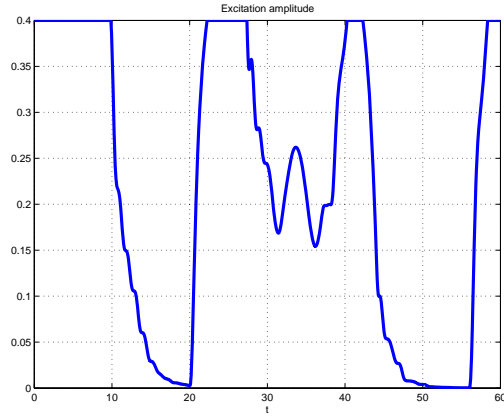


Figure 8. Amplitude of the intelligent excitation.

¹⁹Pomet, J.-B. and Praly, L., "Adaptive Nonlinear Regulation: Estimation from the Lyapunov Equation," *IEEE Transactions on Automatic Control*, Vol. 37, No. 6, June 1992.